Demonstration of the QCCD trapped-ion quantum computer architecture

J. M. Pino,[*] J. M. Dreiling, C. Figgatt, J. P. Gaebler, S. A. Moses, C. H.
Baldwin, M. Foss-Feig, D. Hayes, K. Mayer, C. Ryan-Anderson, and B. Neyenhuis

Honeywell Quantum Solutions
(Dated: March 2, 2020)

We report on the integration of all necessary ingredients of the trapped-ion QCCD (quantum charge-coupled device) architecture into a robust, fully-connected, and programmable trapped-ion quantum computer. The system employs $^{171}Yb^+$ ions for qubits and $^{138}Ba^+$ ions for sympathetic cooling and is built around a Honeywell cryogenic surface trap capable of arbitrary ion rearrangement and parallel gate operations across multiple zones. As a minimal demonstration, we use two spatially-separated interaction zones in parallel to execute arbitrary four-qubit quantum circuits. The architecture is benchmarked at both the component level and at the holistic level through a variety of means. Individual components including state preparation and measurement, single-qubit gates, and two-qubit gates are characterized with randomized benchmarking. Holistic tests include parallelized randomized benchmarking showing that the cross-talk between different gate regions is negligible, a teleported CNOT gate utilizing mid-circuit measurement, and a quantum volume measurement of 2^4.

INTRODUCTION

The first demonstration of a universal set of quantum logic gates were performed with trapped ions [1]. Since then, researchers have demonstrated up to 10 minute coherence times [2], and gate, state preparation, and measurement fidelities surpassing those of other competing quantum computing architectures [3–5]. Upon realizing the basic building blocks of quantum computation, researchers began focusing their attention on how to scale such a machine to the large number of qubits needed for implementing complex quantum algorithms. A crucial feature of trapped-ion based quantum computers is the use of strong motional coupling amongst ions in a crystal to mediate interactions between their internal (qubit) states. While it is possible to make a larger quantum computer simply by putting more ions into a single crystal, this approach is unlikely to be scalable to very large numbers of qubits. Efforts toward trapped-ion quantum computation have therefore focused on architectures that scale the number of ion crystals used and employ quantum communication between the crystals. Methods for inter-crystal communication include using photonic links [6, 7] or physically transporting ions between different crystals. Here we demonstrate the latter approach, which—following the original proposal—we refer to as the QCCD (quantum charge coupled device) architecture [8].

Every proposal for constructing a large-scale quantum computer has engineering challenges, and the QCCD architecture is no different. As described in the original paper, difficulties include: (1) constructing a device capable of trapping a large number of small ion crystals, (2) reordering and precise positioning of ion crystals via fast, robust transport operations, (3) clock synchronization across the inhomogeneous environment of the trap, (4) the likely need for trapping two different ion species, one for use as a qubit and another for sympathetic cooling during the execution of a quantum circuit, and (5) parallelization of both transport and quantum operations across the device. Once these engineering challenges are overcome, the result would be a fully connected quantum processor that benefits from the high gate fidelities demonstrated for small isolated ion crystals *and* has a path to scale to a large number of qubits.

Nearly all of these individual difficulties of the QCCD architecture have been overcome in various laboratories: cryogenic microfabricated surface traps have been built [9], fast transport operations that induce little heating have been demonstrated [10], hyperfine clock-states have been shown to provide a robust qubit with high-fidelity qubit operations [11], and multi-species crystals have been trapped and sympathetically cooled to near their ground state [12]. Combining these features into a single machine creates performance requirements that are seemingly at odds; for example, cross-talk minimization benefits from increasing spatial separation at the cost of magnetic field homogeneity, inter-zone clock synchronization, increased transport distances, and detection optics complexity. Additionally, the system-level integration of challenging and disparate technologies compounds reliability requirements for a functioning device, requiring a whole new framework of automation and robustness.

In this article, we report on the integration of all these necessary ingredients into a full-stack QCCD quantum computer. The device is built around a microfabricated cryogenic surface trap (Fig. 1) containing five zones used for gating operations and ten storage zones. Using $^{171}Yb^+$ and $^{138}Ba^+$ as the qubit and coolant ions, respectively, we demonstrate parallel operation and communication between two adjacent gate zones separated by $750\mu m$. Loading the trap with four ions of each species, we show that high fidelity gate operations can be performed in parallel on two four-ion mixed-species crystals

and that fast transport operations allow the qubits to be reconfigured between those operations in order to execute arbitrary quantum circuits without the overhead of logical swap gates. Using randomized benchmarking we demonstrate high-fidelity single-qubit and two-qubit gates in the two zones and show that the cross-talk error is small. By teleporting a CNOT gate, we demonstrate the ability to perform mid-circuit measurements without damaging the other qubits in the circuit. Finally, we demonstrate the faithful integration of the different components by running a quantum-volume test using all four qubits in these two interaction zones and find a quantum volume of $2^4 = 16$. The demonstration of these technologies integrated together in a single system paves the path for continued scaling of trapped-ion quantum computers.

SYSTEM

Hardware

We designed and fabricated a 2D surface trap with segmented trap electrodes at Honeywell's microfabrication production facility in Plymouth, MN. The photograph and diagram in Fig. 1 shows the RF Paul trap featuring a linear geometry for the simultaneous trapping of multiple linear chains of ions. The trap consists of five zones dedicated to optical gates, two zones dedicated to storage of ions, one zone with a through hole for ion loading, and eight auxiliary zones for storing and sorting ions. Ions are trapped and transported to different regions in the trap via dynamic voltage waveforms that are individually applied to each of the 198 DC electrodes. All five gate zones are capable of the transport required to implement parallel gate operations and detection across the trap. In this work, we use the storage zone closest to the load hole as a gate zone for convenience, as it has all of the necessary capabilities for the required transport. Hereafter, we shall refer to this zone as a gate zone for ease of reference.

The trap was designed for operation in a cryogenic environment and fabricated using gold electrodes with an undercut etch to mitigate stray fields by eliminating line-of-sight between dielectrics and the ions [13]. The trap is cooled to 12.6 K via a cold finger attached to a liquid He flow cryostat with stability better than 2 mK, thereby suppressing gate errors due to anomalous heating [14].

We store quantum information in the $^{171}\text{Yb}^+$ $^2\text{S}_{1/2}$ hyperfine "clock" states, $|0\rangle \equiv |F = 0, m_F = 0\rangle$ and $|1\rangle \equiv |F = 1, m_F = 0\rangle$, with a frequency splitting of 12.642821 GHz [15], where F and m_F are the quantum numbers for total angular momentum and its z-projection. We pair each Yb ion with a partner Ba ion for sympathetic cooling, and throughout a circuit they exist either as a four ion crystal (Ba-Yb-Yb-Ba or Yb-Ba-Ba-Yb) or as a Yb-Ba
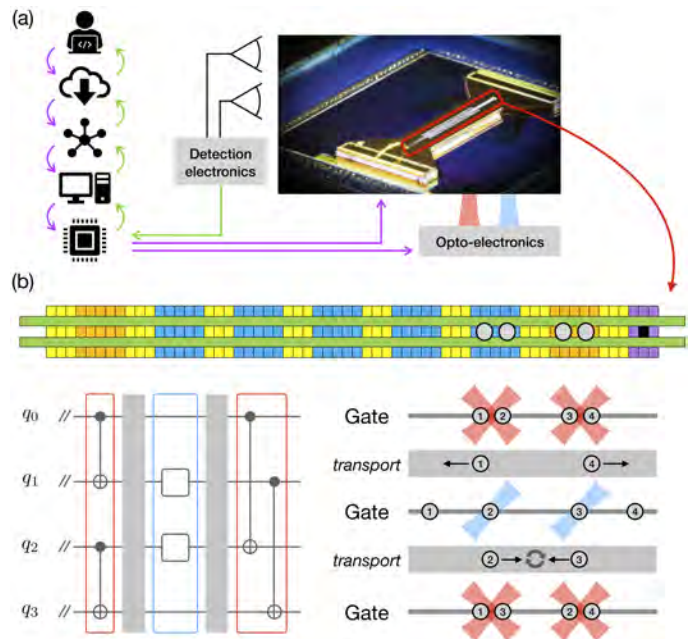

FIG. 1. Illustration of the programmable QCCD quantum computing system along with a photograph of the trap. (a) On the right, a picture of the trap. On the left, the information flow from the user to the trapped qubits. From top to bottom we illustrate: user, cloud, internal tasking, machine control system, FPGA. The circuits are processed by a compiler as described in the text to generate control signals (purple) sent to both the trap electrodes as well as optoelectronic devices that control laser beams. An imaging system and PMT array collects and counts scattered photons, and the result (green) is sent back to the software stack and user. (b) A schematic of the trap detailing: the load hole (black), load zone (purple), storage zones (orange), gate zones (blue), as well as auxiliary zones (yellow) for additional qubit storage. The illustration of how a general quantum circuit is carried out shows that ions already sharing a gate zone are gated, then spatially isolated for single-qubit gates, then the second and third ions are swapped so that the final two-qubit gates can be executed. While not shown, readout, two-qubit gates, and single-qubit rotations can all be performed in parallel.

pair.

The qubits are initialized and measured using standard optical pumping and state-dependent fluorescence techniques [15], and the ions' fluorescence is imaged onto a linear PMT array for quantum circuit measurements. Cooling is accomplished via a combination of Doppler cooling and ground-state Raman sideband cooling [16] of the Ba ions. The ground-state cooling occurs once after initial Doppler cooling and then again immediately before each two-qubit gate. Gating operations are accomplished via stimulated Raman transitions driven by two different configurations: single-qubit gates are implemented using pairs of co-propagating 370.3 nm Raman beams with circular polarization, and two-qubit gates are implented with additional pairs of beams that couples to

an axial mode of motion (along the trapping RF-null).

We impose a quantization axis parallel to the trap surface at a 45° angle with respect to the RF-null. This 5 G field is uniform between the two zones to within 0.2 mG, creating non-uniformity in the measured qubit frequencies of less than 1 Hz. All laser systems are frequency and intensity stabilized via closed-loop feedback, and all beam alignment is handled through automated routines.

Computer Control

We illustrate the software stack from the user down to the qubits in Fig. 1. The processor is programmed using the quantum circuit model [17]. A quantum circuit is submitted remotely through a cloud-based service and tasked in Honeywell's internal cloud. The algorithm is compiled into the various primitives needed to execute the quantum circuit and sent to the machine control system. This system is responsible for programming the field-programmable gate array (FPGA) to execute the specific quantum circuit as well as scheduling and executing calibration routines. These automated calibrations are either executed on a predetermined time interval or triggered when a drift tolerance is exceeded. The FPGA handles the timing of operational primitives and real-time decision-making based on mid-circuit measurement outcomes. Clock synchronization between qubits is maintained via a phase-tracking protocol handled by the FPGA, which updates the qubit phases after transport and gate operations to account for phase accumulation generated by AC-Stark shifts.

In the rare event of ion-loss or detectable ion-reordering events, the data is discarded at the machine control level, and circuits are repeated as necessary to produce valid data. Finally, results are reported back through the cloud service to the user.

PRIMITIVE OPERATIONS

Trapping and transport

A hole in the trap, shown in Fig. 1, allows a collimated beam of neutral atoms from an effusive thermal source to enter the trapping region. To load the device, these atoms are photoionized and Doppler cooled using standard techniques [15] and then transported to one of the gate zones. We initialize the quantum registers with a Ba-Yb-Yb-Ba crystal in two of the gate zones in Fig. 1. To enable all-to-all connectivity and entangle any two qubits, a suite of transport operations, achieved by applying dynamic waveforms to the DC electrodes, allows the order of the ions to be arbitrarily rearranged. These transport operations fall into three categories:
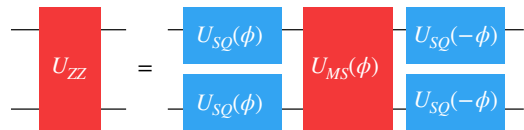

FIG. 2. Construction of a phase-insensitive two-qubit gate. The Mølmer-Sørensen interaction generates the unitary $U_{MS} = \exp(-i\frac{\pi}{4}(X\sin\phi + Y\cos\phi)^{\otimes 2})$ whose basis is determined by the optical phase ϕ. Single-qubit operations driven by the same laser beams generate the unitary $U_{SQ} = \exp(-i\frac{\pi}{4}(X\cos\phi + Y\sin\phi))$ and are applied globally to both qubits. The resulting composite gate is, up to a global phase, equal to $U_{zz} = \exp(-i\frac{\pi}{4}Z \otimes Z)$.

Linear transport: A potential well is moved along the RF-null from one region of the trap to another [18]. During loading, we transport a single ion in a single well; however, during a quantum-circuit, multiple wells at different axial positions are moved simultaneously. Note that in our architecture, these linear transports always involve moving a Yb-Ba pair.

Split/combine: During a split operation, a single potential well is divided into two potential wells [19], splitting a 4-ion crystal into two 2-ion crystals. The combine operation is the time-reversal of the split operation, and both occur only in the gate zones.

Swap: The qubit order of a 4-ion crystal is flipped by rotating the qubits about an axis perpendicular to the RF-null [20]. These operations only occur in gate zones and allow us to avoid the quantum circuitry overhead of logical swaps.

These three transport primitives can be used to arbitrarily rearrange the qubits in a quantum circuit. On average, these transport primitives add less than two quanta of heating axially. Transport failure events are rare and, as previously stated, are automatically detected and scrubbed from the data sets so that computations are not corrupted. A typical duration to reconfigure the ion locations through transport and re-cool them to near the motional ground state is 3-5 ms. This time scale can be reduced via faster and more precise transport operations with improved electrode-control electronics as well as optimized waveforms and electrode geometries.

Quantum Operations

For qubit initialization and measurement, we spatially isolate a single Yb-Ba crystal so that resonant scattered light has a minimal effect on the other qubits. This allows measurement (and subsequent initialization, if necessary) to be performed at any point in the circuit. Our native gate set consists of four basic types of gates:

Single-qubit Z rotations: The single-qubit rotation around Z is done entirely in software by a phase-tracking
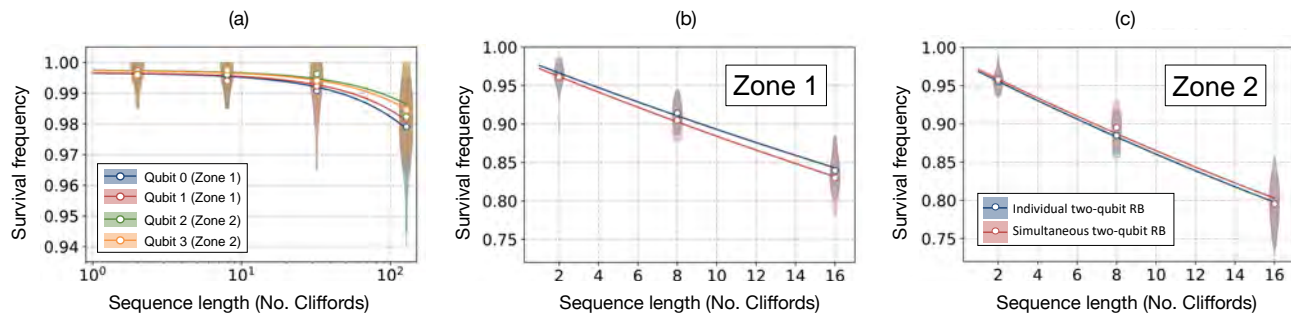
FIG. 3. (a) Single-qubit randomized benchmarking for all four qubits. (b,c) Two-qubit randomized benchmarking results for both zones. We performed two-qubit randomized benchmarking in each zone, both separately and simultaneously and observe no statistically significant difference between the two sets of experiments. This indicates that cross-talk errors do not play a significant role in our two-qubit gates (see the Appendix for more details).

update as described in the Computer Control section. We set a resolution limit of $\pi/500$ for Z rotations.

Single-qubit X/Y rotations: Stimulated Raman transitions on an isolated Yb-Ba crystal in a gate zone are used to apply single-qubit rotations about an arbitrary axis in the X-Y plane. The transition is driven by the co-propagating single-qubit beams described in the Hardware section. We currently restrict our gate set to π and $\pi/2$ rotations. Arbitrary single-qubit gates submitted by the user are synthesized into at most two X/Y rotations along with an additional Z-rotation.

Two-qubit gates: We operate a Mølmer-Sørensen interaction [21] in the phase-sensitive configuration [22], and add single-qubit wrapper pulses driven with the same lasers (Fig. 2) to remove the optical phase dependence, resulting in the phase-insensitive entangling gate $U_{zz} = \exp(-i\frac{\pi}{4}Z \otimes Z)$.

Global microwave rotations: A microwave antenna in the vacuum chamber applies global qubit rotations with a variable phase. The microwave field amplitude is only homogeneous over the entire device to within about 3% and, therefore, not suitable for logical operations in a quantum circuit. We do, however, use microwaves to suppress memory errors through dynamical decoupling [23]. Since the amplitude is inhomogeneous we cannot apply global microwave π pulses, as is the nominal prescription for dynamical decoupling. In order to avoid the accumulation of coherent errors, we apply pulses in pairs with opposite phases during ground-state cooling without any transport operation in between, thereby canceling out small amplitude errors while mostly preserving the memory error suppression benefits.

SYSTEM PERFORMANCE

To characterize the system, we evaluate the individual components and then compare the results to several holistic measurements.

Component benchmarking

We benchmark single-qubit gates, our native two-qubit gate, and state preparation and measurement (SPAM) using randomized benchmarking (RB). Results of each component benchmark are summarized in Table I. Further details on each procedure are given below:

State preparation and measurement: We extract a SPAM error from the y-intercept of the survival probability in single-qubit RB. Theoretical modeling suggests the error from state preparation via optical pumping is below 10^{-4}, whereas the effective solid angle of our photon-detectors currently limits the measurement error to $> 10^{-3}$. Thus, we believe SPAM errors are dominated by measurement error.

Single-qubit gates: We simultaneously perform single-qubit RB with each qubit following the standard Clifford-twirl version of RB outlined in Ref. [24], with results plotted for each qubit in Fig. 3a.

Two-qubit gate: We perform two-qubit RB in each zone independently and then again simultaneously in both zones, following the standard Clifford-twirl version of RB [24]. Results are plotted in Fig. 3(b,c), and we report the average infidelity of the two-qubit Clifford gates scaled by the average number of U_{zz} gates (1.5).

We also perform the simultaneous RB method, as described in Ref. [25], generalized to two-qubit RB. This method has two parts: (1) identify differences in RB decay rates between applying gates individually and simultaneously, and (2) identify correlated errors when applying gates simultaneously (also similar to Ref. [26]). From both analyses, we find no statistically significant evidence of cross-talk errors (see the Appendix). While this method does not capture all possible cross-talk errors, we believe it is a strong indication that these type of errors are minimal in this system.

Component	Zone Avg.	Zone 1	Zone 2
SPAM (simultaneous SQ RB)	$3(1) \times 10^{-3}$	$[3(1) \times 10^{-3}, 3(1) \times 10^{-3}]$	$[2(1) \times 10^{-3}, 3(1) \times 10^{-3}]$
Single-qubit gates (simultaneous RB)	$1.1(3) \times 10^{-4}$	$[1.4(3) \times 10^{-4}, 1.2(2) \times 10^{-4}]$	$[9(2) \times 10^{-5}, 1.0(3) \times 10^{-4}]$
Two-qubit gates (individual RB)	$7.9(4) \times 10^{-3}$	$6.7(5) \times 10^{-3}$	$9.0(4) \times 10^{-3}$
Two-qubit gates (simultaneous RB)	$8.0(4) \times 10^{-3}$	$7.2(4) \times 10^{-3}$	$8.8(4) \times 10^{-3}$

TABLE I. Summary of component benchmarking results. Numbers are the average error per operation. For SPAM and single-qubit gates, the two numbers represent the measured values for each qubit in the corresponding zone.

Mid-circuit measurement

Splitting and spatially isolating ion-crystals enables measurement of a single qubit in the middle of a circuit without damaging the quantum information stored in the other qubits. This capability, along with the ability to reinitialize the qubit after it is measured, enables several new algorithmic capabilities including quantum error correction [17]. Recently, the NIST group demonstrated mid-circuit measurements through a teleported CNOT gate circuit [27], which we use as our algorithmic benchmark for this primitive.

Quantum gate teleportation is a protocol in which a pair of maximally entangled qubits is used as a resource for applying a gate between a pair of remote data qubits [28]. The protocol requires local entangling operations, mid-circuit measurements, and classically-conditioned quantum gates. The circuit for teleportation of the CNOT gate is shown in Fig. 4a. Here, qubits q_1 and q_2 are initially prepared in the Bell state $|\psi_B\rangle = \frac{1}{\sqrt{2}}\big(|00\rangle + |11\rangle\big)$. Two rounds of CNOT gates, each followed by a measurement and conditional gate, result in a circuit that is logically equivalent to a CNOT controlled on q_0 and targeting q_3 (see Fig. 4). To realize this circuit, transport operations are required to distribute the Bell state between two zones for remote gating. Each CNOT in the circuit is compiled into a native U_{zz} gate and single-qubit rotations.

To efficiently benchmark the teleported CNOT gate, we use the method of Ref. [29] for bounding the fidelity of a process from its action on two mutually-unbiased bases. This amounts to verifying the following quantum truth table:

$$CNOT: \begin{array}{ll} |00\rangle \mapsto |00\rangle, & |++\rangle \mapsto |++\rangle, \\ |01\rangle \mapsto |11\rangle, & |+-\rangle \mapsto |+-\rangle, \\ |10\rangle \mapsto |10\rangle, & |-+\rangle \mapsto |--\rangle, \\ |11\rangle \mapsto |01\rangle, & |-+\rangle \mapsto |--\rangle, \end{array}$$

where the states are labeled $|q_3 q_0\rangle$. We prepare q_0 and q_3 in each state of the $\{|0\rangle, |1\rangle\}$ and $\{|+\rangle, |-\rangle\}$ bases, apply the circuit in Fig. 4a and measure in the appropriate basis. We repeat the circuit 500 times for each input state, and randomize the order in which the eight variations are run. The data is shown in Fig. 4b.

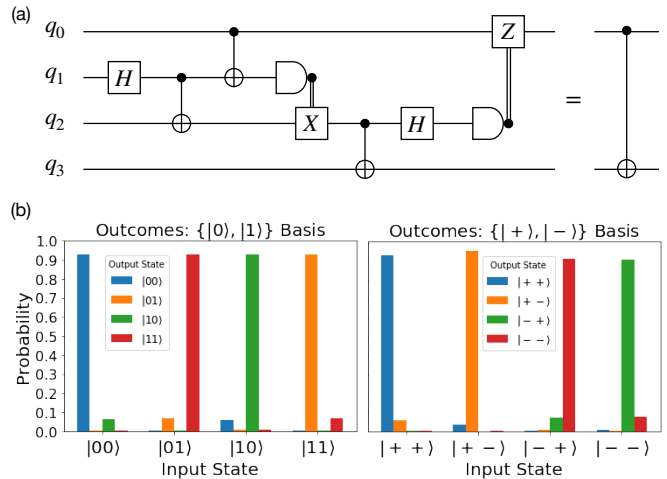Let f_1 and f_2 be the average success probabilities over

FIG. 4. (a) Circuit implementing a teleported CNOT gate, with q_0 and q_3 the control and target qubits, respectively. (b) Bar plots showing the distribution of measurement outcomes when qubits q_0 and q_3 are prepared and measured in the $\{|0\rangle, |1\rangle\}$ and $\{|+\rangle, |-\rangle\}$ bases.

the $\{|0\rangle, |1\rangle\}$ and $\{|+\rangle, |-\rangle\}$ bases, respectively. The average fidelity F_{avg}[30] of the teleported CNOT gate is lower bounded according to

$$F_{\mathrm{avg}} \geq \frac{4}{5}\big(f_1 + f_2\big) - \frac{3}{5}. \tag{1}$$

This bound does not account for errors in the state preparations and measurements required for benchmarking. However, since these errors are much smaller than the full circuit error, Eq. (1) serves as a useful proxy for the circuit performance. We find $f_1 = 0.933(6)$ and $f_2 = 0.941(5)$, yielding $F_{\mathrm{avg}} \geq 0.899(6)$.

Quantum Volume

Quantum volume (QV) is a full-circuit benchmark that is dependent on both qubit number and gate fidelity [31]. By weighing both metrics, QV attempts to estimate the effective power of the quantum computer. In practice, a QV test consists of running random $O(n)$ depth circuits with n qubits, as shown in Fig. 5a for $n = 4$. This makes QV sensitive to errors that may be missed by some
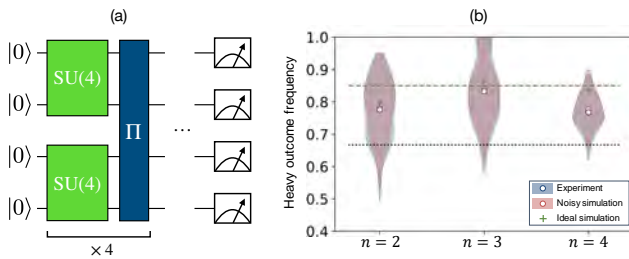
FIG. 5. (a) Quantum volume circuits for $n = 4$. As described in Ref. [31], the test is run by interleaving random SU(4) gates, which each require three entangling gates, with random permutations of qubits (denoted Π). While some architectures will need to use quantum logic gates for the permutations, the QCCD architecture can use physical swap operations that have a negligible effect on the stored quantum information. (b) Results for QV test for $n = 2, 3$ and 4. For each test we performed 100 randomly generated circuits from Qiskit repeated 500 times each with distribution over circuits plotted in blue. We also ran a noisy simulation in Qiskit with depolarizing errors with rates estimated from RB experiments, which are plotted in red. The average of the ideal outcomes for the 100 circuits run are given by green crosses. The green dashed line is the average over all ideal circuits while the black dashed line gives the passing threshold.

component benchmarks and could degrade performance in generic computations. The circuits are then classically simulated and the measured outputs are tested against the heavy-outcome criteria. If the circuits pass this test 2/3's of the time with two sigma confidence, then the system is said to have $QV = 2^n$.

We performed the QV test for $n = 2, 3$, and 4, each with 100 random circuits generated by Qiskit [32]. We passed QV for $n = 2$ with 77.58% of the circuits and 99.56% confidence, $n = 3$ with 83.28% of the circuits with 99.9996% confidence, and $n = 4$ with 76.77% of the circuits and 99.16% confidence (results are plotted in Fig. 5b). All confidence intervals are calculated from the method outlined in Ref. [31]. Each QV circuit was run without any optimization or approximations. For example, in the $n = 4$ test each circuit contained exactly 24 two-qubit gates.

Fig. 5 also shows theoretical simulations of the circuit outcomes assuming a depolarizing noise channel for the two-qubit gates, with a noise magnitude extracted from two-qubit RB. The excellent agreement provides further evidence that the QCCD architecture fulfills its most ambitious goal: maintaining the gate fidelities achievable in small ion crystals while executing arbitrary circuits on multiple qubits.

DISCUSSION

The goal of this manuscript has been to present and validate a realization of the QCCD architecture, and to benchmark the full set of required operations. Two gate zones were operated in parallel to execute arbitrary quantum circuits on 4 qubits, and we have shown evidence that coherence times, transport reliability, and robust sympathetic cooling are sufficient to execute large depth circuits.

Together with the verification of extremely low cross-talk between neighboring gate zones, these results suggest a path forward in which the primary near-term obstacles to scalability are technical in nature and generally less severe than those already overcome in the work presented here. We are currently pursuing a scaling of the optical delivery to encompass all 5 gates zones, and even without further improvements to gate fidelities we expect to increase the accessible quantum volume. Finally, while we recognize the challenges ahead, we believe the successful integration of QCCD primitives demonstrated in this manuscript paves the way toward near-term intermediate-scale devices with fidelities approaching state-of-the-art demonstrations in small ion crystals.

* juan.pino@honeywell.com

[1] C. Monroe, D. M. Meekhof, B. E. King, W. M. Itano, and D. J. Wineland, Phys. Rev. Lett. **75**, 4714 (1995).

[2] Y. Wang, M. Um, J. Zhang, S. An, M. Lyu, J.-N. Zhang, L.-M. Duan, D. Yum, and K. Kim, Nat. Photonics **11**, 646 (2017).

[3] J. P. Gaebler, T. R. Tan, Y. Lin, Y. Wan, R. Bowler, A. C. Keith, S. Glancy, K. Coakley, E. Knill, D. Leibfried, and D. J. Wineland, Phys. Rev. Lett. **117**, 060505 (2016).

[4] C. J. Ballance, T. P. Harty, N. M. Linke, M. A. Sepiol, and D. M. Lucas, Phys. Rev. Lett. **117**, 060504 (2016).

[5] J. E. Christensen, D. Hucul, W. C. Campbell, and E. R. Hudson, "High fidelity manipulation of a qubit built from a synthetic nucleus," (2019), arXiv:1907.13331 [quant-ph].

[6] C. Monroe, R. Raussendorf, A. Ruthven, K. R. Brown, P. Maunz, L.-M. Duan, and J. Kim, Phys. Rev. A **89**, 022317 (2014).

[7] D. Hucul, I. V. Inlek, G. Vittorini, C. Crocker, S. Debnath, S. M. Clark, and C. Monroe, Nat. Phys. **11**, 37 (2015).

[8] D. Kielpinski, C. Monroe, and D. J. Wineland, Nature **417**, 709 (2002).

[9] J. Labaziewicz, *High Fidelity Quantum Gates with Ions in Cryogenic Microfabricated Ion Traps*, Ph.D. thesis, MIT (2008).

[10] R. Bowler, J. Gaebler, Y. Lin, T. R. Tan, D. Hanneke,

J. D. Jost, J. P. Home, D. Leibfried, and D. J. Wineland, Phys. Rev. Lett. **109**, 080502 (2012).

[11] C. Langer, R. Ozeri, J. D. Jost, J. Chiaverini, B. De-Marco, A. Ben-Kish, R. B. Blakestad, J. Britton, D. B. Hume, W. M. Itano, D. Leibfried, R. Reichle, T. Rosen-band, T. Schaetz, P. O. Schmidt, and D. J. Wineland, Phys. Rev. Lett. **95**, 060502 (2005).

[12] M. D. Barrett, B. DeMarco, T. Schaetz, V. Meyer, D. Leibfried, J. Britton, J. Chiaverini, W. M. Itano, B. Jelenković, J. D. Jost, C. Langer, T. Rosenband, and D. J. Wineland, Phys. Rev. A **68**, 042302 (2003).

[13] P. L. W. Maunz, SAND2016-0796R (2016), 10.2172/1237003.

[14] J. Labaziewicz, Y. Ge, D. R. Leibrandt, S. X. Wang, R. Shewmon, and I. L. Chuang, Phys. Rev. Lett. **101**, 180602 (2008).

[15] S. Olmschenk, K. C. Younge, D. L. Moehring, D. N. Mat-sukevich, P. Maunz, and C. Monroe, Phys. Rev. A **76**, 052314 (2007).

[16] C. Monroe, D. M. Meekhof, B. E. King, S. R. Jefferts, W. M. Itano, D. J. Wineland, and P. Gould, Phys. Rev. Lett. **75**, 4011 (1995).

[17] M. A. Nielsen and I. L. Chuang, *Quantum Computation and Quantum Information* (Cambridge University Press, 2000).

[18] M. Palmero, R. Bowler, J. P. Gaebler, D. Leibfried, and J. G. Muga, Phys. Rev. A **90**, 053408 (2014).

[19] J. P. Home and A. M. Steane, Quantum Information and Computation **6**, 289 (2006).

[20] F. Splatt, M. Harlander, M. Brownnutt, F. Zahringer, R. Blatt, and W. Hansel, New Journal of Phyics **11**, 103008 (2009).

[21] A. Sørensen and K. Mølmer, Phys. Rev. A **62**, 022311 (2000).

[22] P. J. Lee, K.-A. Brickman, L. Deslauriers, P. C. Haljan, L.-M. Duan, and C. Monroe, Journal of Optics B: Quantum and Semiclassical Optics **7**, S371 (2005).

[23] L. Viola, E. Knill, and S. Lloyd, Phys. Rev. Lett. **82**, 2417 (1999).

[24] E. Magesan, J. M. Gambetta, and J. Emerson, Phys. Rev. Lett. **106**, 180504 (2011).

[25] J. M. Gambetta, A. D. Córcoles, S. T. Merkel, B. R. Johnson, J. A. Smolin, J. M. Chow, C. A. Ryan, C. Rigetti, S. Poletto, T. A. Ohki, M. B. Ketchen, and M. Steffen, Phys. Rev. Lett. **109**, 240504 (2012).

[26] R. Harper, S. T. Flammia, and J. J. Wallman, "Efficient learning of quantum noise," (2019), arXiv:1907.13022 [quant-ph].

[27] Y. Wan, D. Kienzler, S. D. Erickson, K. Mayer, T. R. Tan, J. J. Wu, H. M. Vasconcelos, S. Glancy, E. Knill, D. J. Wineland, A. C. Wilson, and D. Leibfried, Science **364**, 875 (2019).

[28] J. Eisert, K. Jacobs, P. Papadopoulos, and M. B. Plenio, Phys. Rev. A **62**, 052317 (2000).

[29] H. F. Hofmann, Phys. Rev. Lett. **94**, 160504 (2005).

[30] M. A. Nielsen, Physics Letters A **303**, 249 (2002).

[31] A. W. Cross, L. S. Bishop, S. Sheldon, P. D. Nation, and J. M. Gambetta, Phys. Rev. A **100**, 032328 (2019).

[32] H. Abraham and *et al.*, "Qiskit: An open-source framework for quantum computing," (2019).

[33] C. H. Baldwin, B. J. Bjork, J. P. Gaebler, D. Hayes, and D. Stack, "Subspace benchmarking high-fidelity entangling operations with trapped ions," (2019), arXiv:1911.00085 [quant-ph].

[34] R. Harper, I. Hincks, C. Ferrie, S. T. Flammia, and J. J. Wallman, Phys. Rev. A **99**, 052350 (2019).

[35] A. M. Meier, *Randomized Benchmarking of Clifford Operators*, Ph.D. thesis, University of Colorado (2006), arXiv:1811.10040 [quant-ph].

Zone	α_z	α_z^{both}	γ_z
1	0.9866(9)	0.9856(8)	$9(10) \times 10^{-4}$
2	0.9820(8)	0.9824(8)	$4(12) \times 10^{-4}$

TABLE II. Addressability error estimates for simultaneous RB.

Simultaneous two-qubit randomized benchmarking

Simultaneous RB was originally proposed in Ref. [25] to measure addressability in single-qubit gates, and here we describe the extension to two-qubit gates. Two-qubit simultaneous RB is performed by three experiments: (1) RB in zone one while doing no gates in zone two, (2) RB in zone two while doing no gates in zone one, and (3) RB in both zones simultaneously.

For reference, we fit the RB data to the zeroth order RB decay equation

$$p(\ell) = A\alpha^\ell + B, \qquad (2)$$

where $p(\ell)$ is the average survival frequency for a length ℓ RB sequence, A is the SPAM parameter, α is the RB decay rate, and B is the asymptote, which is typically fixed by randomization of the final measurement [33, 34]. We then calculate the uncertainty by finding the standard deviation of a semi-parametric bootstrap resample outlined in Ref. [35] and also used in Ref. [33].

The data is then analyzed in two steps:

Addressability analysis: Addressability errors are induced in one zone from operations in the other zone. For example, if laser light from zone one is leaking into zone two that will cause an error in zone two but not zone one. Addressibility errors are measured by comparing the difference between the decay rates in each zone in experiments one and two, defined as α_z for $z = 1, 2$, and the decay rates in each zone from experiment three and α_z^{both} [25],

$$\gamma_z = |\alpha_z - \alpha_z^{\text{both}}|. \qquad (3)$$

We compare the decay rates instead of the fidelity as done in Ref. [25]. As summarized in Table II, we see that the measured values of γ_z are within one standard deviation of zero.

Correlation analysis: Correlation errors are those that are shared between the zones when running RB simultaneously. For example, if the laser power changes when applying gates to both zones this will cause an error in both zones. In Ref. [25] it was shown that these
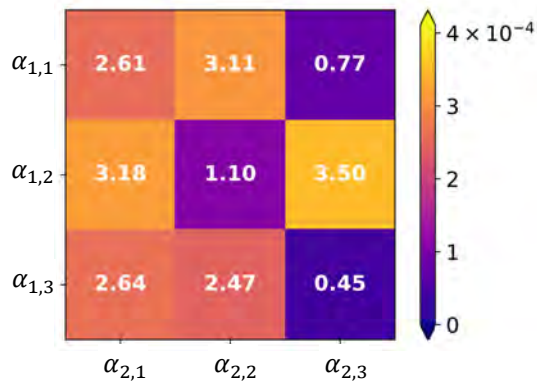
FIG. 6. Correlation parameters for simultaneous two-qubit RB. Each square in the plot represents a value of $\delta_{i,j}$ with numbers scaled by 10^{-4}. Each parameter is within one standard deviation of zero.

types of errors can be identified by studying different outcomes in simultaneous RB experiments. They identified the group structure of the two subsystem Clifford group $C_1^{\otimes 2}$ and showed that it leads to three distinct decay rates α_1, α_2, and β (with 'both' superscript dropped since we only consider simultaneous RB experiments for this analysis). The first two decays correspond to errors on each individual qubit but the third decay corresponds to correlated errors. If the simultaneous gates do not cause any additional correlated errors, then $\alpha_1\alpha_2 = \beta$. However, if additional correlated errors exist, then $\alpha_1\alpha_2 \leq \beta$. The magnitude of the error is then defined as,

$$\delta = \alpha_1\alpha_2 - \beta. \tag{4}$$

For parallel two-qubit gates, things are more complicated due to the group structure of $C_2^{\otimes 2}$. There are 15 different decay rates, including six that correspond to the individual two-qubit subsystems $\alpha_{z,i}$ for $i = 1, 2, 3$, and 9 that correspond to correlated errors $\beta_{i,j}$ for $i, j = 1, 2, 3$. Physically, these correspond to different types of correlated errors that affect the different combinations of the four total qubits. To quantify the correlation errors we calculate,

$$\delta_{i,j} = |\alpha_{1,i}\alpha_{2,j} - \beta_{i,j}|. \tag{5}$$

The results are summarized in Fig. 6, which plots $\delta_{i,j}$ for all 9 values. The minimum standard deviation over all correlation parameters estimated from the semi-parametric bootstrap is 4.1×10^{-4}. Therefore, we see that all correlation parameters are within one standard deviation of zero.

Simultaneous two-qubit RB indicates that addressability and correlation errors are consistent with zero with high-confidence. However, this does not mean *all* cross-talk errors are zero in the system. Cross-talk is a broad term and may refer to any context dependence of the system when parallel gates are applied. This could include errors that are missed with these experiments. For example, there may be errors present that do not change the average fidelity of an RB experiment but still cause different effects in an arbitrary quantum circuit. However, from this analysis we see that the effect of cross-talk with random circuits is small and likely has a minimal effect in typical circuits. This conclusion is further verified with other example algorithms like QV.